J. Fluid Mech. (2006), *vol.* 546, *pp.* 193–202.
doi:10.1017/S0022112005007433 Printed in the United Kingdom

Axisymmetric stability of the flow between two exactly counter-rotating disks with large aspect ratio

By L. MARTIN WITKOWSKI[1,2], I. DELBENDE[1,2], J. S. WALKER[3] AND P. LE QUÉRÉ[2]

[1]Université Paris VI, 4 place Jussieu, F-75252 Paris Cedex 05, France

[2]LIMSI-CNRS, UPR 3251, BP 133, F-91403 Orsay Cedex, France

[3]Department of Mechanical and Industrial Engineering, University of Illinois, 1206 W. Green St., Urbana, IL 61801, USA

(Received 21 June 2005 and in revised form 29 September 2005)

We study the first bifurcation in the axisymmetric flow between two exactly counter-rotating disks with very large aspect ratio $\Gamma \equiv R/H$, where R is the disk radius and $2H$ is the inter-disk spacing. The scaling law for the critical Reynolds number is found to be $Re_c \propto \Gamma^{-1/2}$, with $Re \equiv \Omega H^2/\nu$, Ω being the magnitude of the angular velocity and ν the kinematic viscosity. An asymptotic analysis for large Γ is developed, in which curvature is neglected, but the centrifugal acceleration term is retained. The Navier–Stokes equations then reduce to leading order to those in a Cartesian frame, and the axisymmetric base flow to a parallel flow. This allows us locally to use a Fourier decomposition along the radial direction. In this framework, we explain the physical mechanism of the instability invoking the linear azimuthal velocity profile and the effect of centrifugal acceleration.

1. Introduction

The flow between two parallel rotating disks with very large aspect ratio can be thought of as an approach to plane Couette flow with additional degrees of freedom, namely curvature and background rotation, given by the mean angular velocity of the disks. This analogy has been presented for the rotor–stator system by Schouveiler, Le Gal & Chauve (2001). Hoffmann, Busse & Chen (1998) investigated the stability of plane Couette flow (i.e. zero curvature) with background rotation. The present paper is devoted to the case of exactly counter-rotating disks, for which background rotation is zero. An experiment on this configuration has been carried out by J. Pécheux and E. Foucault (private communication). These authors covered numerically a range of aspect ratios Γ (disk radius/ half spacing between the disks) varying from 20 to 80 and performed an experiment for $\Gamma = 30$. They showed that an instability occurs at a very small rotation rate of the disks so that the profile of the azimuthal velocity for the base flow is almost linear in the axial direction. The observed patterns of the instability are strongly dominated by an axisymmetric propagating wave. Another feature of this instability is that the spatial wavelength is of the order of the disk spacing and the structures extend from one disk to the other. These patterns differ from those presented by Nore *et al.* (2004) for small aspect ratio ($\Gamma < 4$) which are three-dimensional and stationary. They are also different from boundary layer instabilities over a rotating disk, which still receive much attention (Lingwood 1997;

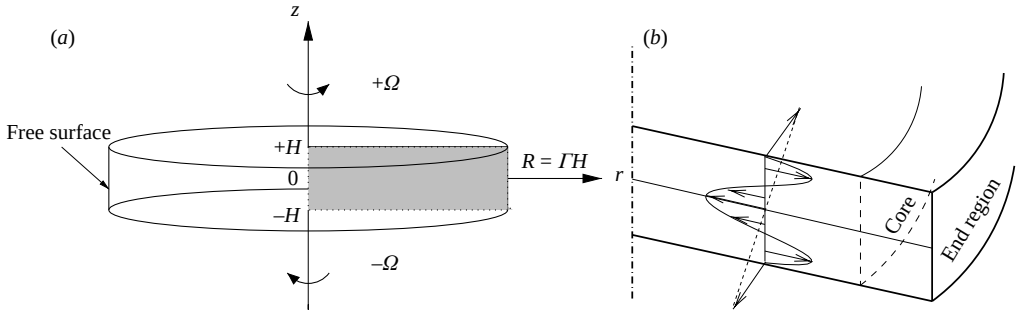

FIGURE 1. (*a*) Sketch of the configuration using dimensional variables. (*b*) Base flow: schematic representation of the azimuthal and radial velocities in the core region.

Fernandez-Feria 2000; Serre, Tuliszka-Sznitko & Bontoux 2004). Similar instabilities, i.e. for a base flow without boundary layers, have been observed by Schouveiler *et al.* (2001) in an experiment with a rotating and a stationary disk but those instabilities are spiral waves and become critical only for $\Gamma > 112$. An experimental setup with counter-rotating disks is described in Soong *et al.* (2003) but $\Gamma = 25$ is the largest aspect ratio studied and the instability found by J. Pécheux and E. Foucault will not be triggered. Gauthier *et al.* (2002) performed measurements for $\Gamma = 41.8$, but did not reach exact counter-rotation. They observed a transition toward slightly inclined spirals rolling up to the centre in the direction of the slower disk and propagating toward the periphery. In numerical simulations, the difficulty lies in the two very different length scales used to mesh the domain. This geometry is suitable for a semi-analytical study whereby the self-similar solutions for the basic flow between disks of infinite radius are used. Szeto (1978) performed such a study, but enforced the similarity conditions on the perturbation variables as well; this constraint is too strong and leads to critical Reynolds number values much larger than those found experimentally. Our goal is to generalize the study by J. Pécheux and E. Foucault in the limit of infinite Γ and to remove similarity constraints on perturbations used in Szeto (1978). The approach is both numerical and semi-analytical.

In § 2, we present the problem formulation, show the results of the purely numerical approach, compare with experimental results for $\Gamma = 30$ and find the scaling law of the critical Reynolds numbers as a function of Γ. In § 3, we derive for large values of Γ a set of asymptotic equations that can be considered as a local parallel approximation of the original problem; an explanation of the mechanism of the instability is then proposed and a spatio-temporal analysis of the asymptotic equations is used to recover the results found in § 2.

2. Axisymmetric numerical approach

2.1. *Problem formulation*

We use cylindrical coordinates r, θ, z with the z-axis normal to the disks, with the origin at the symmetry plane and unit vectors $\boldsymbol{e}_r, \boldsymbol{e}_\theta, \boldsymbol{e}_z$. We enforce a stress-free boundary condition located at a radius R and the distance between the disks is $2H$. The geometry is presented in figure 1(*a*).

We normalize length by H and velocity by ΩH, where $\pm\Omega$ is respectively the upper and lower disk angular velocity. Based on these scales, we introduce the Reynolds number $Re = \Omega H^2/\nu$ where ν is the kinematic viscosity of the fluid.

Assuming axisymmetry, we use the vorticity $\omega = \partial u_r/\partial z - \partial u_z/\partial r$, streamfunction ψ formulation where $\nabla \times (-\psi\, \boldsymbol{e}_\theta/r) = (u_r, 0, u_z)$ and the velocity $\boldsymbol{V} = (u_r, u_\theta, u_z)$. The Navier–Stokes equations are

$$\frac{\partial \omega}{\partial t} + \frac{\partial (u_r \omega)}{\partial r} + \frac{\partial (u_z \omega)}{\partial z} - \frac{\partial}{\partial z}\left(\frac{u_\theta^2}{r}\right) = \frac{1}{Re}\left(\frac{\partial^2 \omega}{\partial r^2} + \frac{1}{r}\frac{\partial \omega}{\partial r} - \frac{\omega}{r^2} + \frac{\partial^2 \omega}{\partial z^2}\right), \tag{2.1}$$

$$\frac{\partial^2 \psi}{\partial r^2} - \frac{1}{r}\frac{\partial \psi}{\partial r} + \frac{\partial^2 \psi}{\partial z^2} = r\omega, \tag{2.2}$$

$$\frac{\partial u_\theta}{\partial t} + \frac{\partial (u_r u_\theta)}{\partial r} + \frac{2 u_r u_\theta}{r} + \frac{\partial (u_z u_\theta)}{\partial z} = \frac{1}{Re}\left(\frac{\partial^2 u_\theta}{\partial r^2} + \frac{1}{r}\frac{\partial u_\theta}{\partial r} - \frac{u_\theta}{r^2} + \frac{\partial^2 u_\theta}{\partial z^2}\right). \tag{2.3}$$

The boundary conditions are $\psi = 0$, $\partial\psi/\partial z = 0$ and $u_\theta = \pm r$ at $z = \pm 1$ and $\psi = 0$, $\omega = 0$, $\partial u_\theta/\partial r - u_\theta/r = 0$ at $r = \Gamma$. The boundary condition at the periphery could have been chosen differently (e.g. no-slip, open end) but as explained in § 3 a different choice would only influence our present analysis slightly. The stress-free boundary condition usually relates to crystal growth applications and we herein follow Harriott & Brown (1984). In addition to comparisons with these authors, the main advantage of this boundary condition is to preserve symmetry and to avoid any singularity due to discontinuous velocities.

We introduce for ψ the form

$$\psi = \psi_b(r, z) + \epsilon\ Re[\psi_p(r, z) \exp(\lambda t)], \tag{2.4}$$

and a similar form is introduced for u_θ. The subscript b denotes the variables for the steady axisymmetric base flow, the subscript p denotes the complex perturbation eigenfunctions such as $\psi_{pR} + \mathrm{i}\psi_{pI}$, and $\lambda = \lambda_R + \mathrm{i}\lambda_I$ is the complex eigenvalue. The forms for u_r, u_z, ω are deduced directly from ψ.

For the base flow, we use a symmetry condition at mid-plane, namely $\psi_b = 0$, $\omega_b = 0$, $u_{\theta b} = 0$ at $z = 0$ and need only consider the region $0 \leqslant z \leqslant 1$.

For small perturbations, the governing equations are obtained by introducing the form (2.4) into (2.1)–(2.3) and collecting all terms of order ϵ. The boundary conditions at $r = \Gamma$ and $z = 1$ are obtained by the same procedure. Regarding the symmetry at $z = 0$ we need to consider both symmetric (i.e. having the same symmetry as the base flow) and antisymmetric modes. Symmetric perturbations are such that ψ_p, $u_{\theta p}$ are odd functions of z and antisymmetric perturbations are such that ψ_p, $u_{\theta p}$ are even. The use of symmetry for the perturbation equations reduces the size of the computational domain with no loss of generality but implies running two independent calculations: one for the symmetric mode ($\psi_b = 0$, $\omega_b = 0$ and $u_{\theta b} = 0$ at $z = 0$) and one for the antisymmetric mode ($\partial\psi_b/\partial z = 0$, $\partial\omega_b/\partial z = 0$ and $\partial u_{\theta b}/\partial z = 0$ at $z = 0$).

When the aspect ratio is large (typically $\Gamma > 150$) grid resolution becomes a problem. We then restrict the computation to the domain $[\Gamma - \Delta\Gamma, \Gamma] \times [0, 1]$. We assume that the variables satisfy similarity conditions for $r \leqslant \Gamma - \Delta\Gamma$ and therefore prescribe a r and r^2 radial dependence for u_θ and ψ respectively in (2.1)–(2.3). This leads to

$$\frac{\partial \omega}{\partial t} + \frac{2 u_r \omega}{r} + \frac{\partial (u_z \omega)}{\partial z} - \frac{\partial}{\partial z}\left(\frac{u_\theta^2}{r}\right) = \frac{1}{Re}\frac{\partial^2 \omega}{\partial z^2}, \tag{2.5}$$

$$\frac{\partial^2 \psi}{\partial z^2} = r\omega, \tag{2.6}$$

$$\frac{\partial u_\theta}{\partial t} + \frac{4 u_r u_\theta}{r} + \frac{\partial (u_z u_\theta)}{\partial z} = \frac{1}{Re}\frac{\partial^2 u_\theta}{\partial z^2}, \tag{2.7}$$

which we use as boundary conditions at $r = \Gamma - \Delta\Gamma$. The set of equations and boundary conditions are discretized by a standard second-order-accurate finite-difference scheme. All computations presented in § 2.2 are performed on a $[r \times z] = [301 \times 61]$ grid with evenly spaced gridpoints in the z-direction and the mapping function $\Gamma \tanh(\beta r/\Gamma)/\tanh(\beta)$ in the r-direction where β is an arbitrary coefficient. For the full domain code, we set $\beta = 1$ for $\Gamma < 20$ and $\beta = 2$ otherwise. The truncated domain code uses a uniform grid in the r-direction. The procedure to find the base flow and the eigenmodes is described in Martin Witkowski & Walker (2002). We changed the stress-free boundary condition to a no-slip boundary condition at the periphery in order to compare our results with those presented in table 2 of Nore *et al.* (2004) for the axisymmetric mode.† Using a $[161 \times 151]$ uniform grid, we found $Re = 335.3$ for $\Gamma = 2.0$, $Re = 912.7$ for $\Gamma = 1.3\bar{3}$, $Re = 1851$ for $\Gamma = 1.0$, and $Re = 4727$ for $\Gamma = 0.6\bar{6}$ which agree within 2 %, 6 % (but within 2 % with Gelfgat, Bar-Yoseph & Solan 1996), 1 % and 4 % respectively with those of Nore *et al.*

2.2. *Results*

As presented schematically in figure 1(*b*), the base flow consists of an azimuthal and a meridional flow. The azimuthal flow is driven by the moving boundaries. The secondary (meridional) flow is a consequence of the axial variation of the azimuthal velocity. This can be deduced by noticing that the only source term for the secondary flowx is $\partial(u_\theta^2/r)/\partial z$ in (2.1).

For a large but fixed value of Γ, the base flow has the following characteristics as the Reynolds number is increased. For small values of the Reynolds number, the flow is purely viscous and a self-similar von Kármán solution is valid in the entire domain except in an $O(1)$ end region close to $r = \Gamma$. A regular perturbation analysis in the core region leads to the following analytical expression for the base flow:

$$u_{\theta b} = rz + O(Re^2) \text{ and } \psi_b = Re\ r^2\ f(z) + O(Re^3) \text{ with } f(z) = \frac{-z(z^2-1)^2}{60}. \quad (2.8)$$

For intermediate values of the Reynolds number, the core flow is still dominated by viscosity and must match an end region for which inertia can no longer be neglected. For larger values of the Reynolds number, a boundary layer regime starts to develop as described by Batchelor (1951).

For small aspect ratio, the axisymmetric stationary bifurcation has been described by Harriott & Brown (1984). For $\Gamma = 2$, they predicted $Re_c \approx 109$ (to be divided by 4 based on our reference scales) which agrees with our value $Re_c = 27.33$. For a large enough aspect ratio ($\Gamma \geqslant 26.7$), an instability via an Hopf bifurcation is triggered. The perturbed streamfunction consists of pairs of counter-rotating rolls. These travelling waves propagate from the axis toward the end region. The amplitude of the perturbed streamfunction is extremely small close to the axis, then steeply increases with r as the rolls reach the end region and finally drops to zero at $r = \Gamma$ due to boundary conditions at the stress-free surface. The instability is antisymmetric, ψ_p and $u_{\theta p}$ being even functions of z. The patterns observed are in good agreement with the experimental ones (J. Pécheux and E. Foucault, private communication) and critical values of both the Reynolds number and frequency are in the same range. For $\Gamma = 30$, they reported a critical $Re_c = 5.75$ and $\lambda_{Ic} = -2.5 \pm 0.1$; we found $Re_c = 5.16$ and $\lambda_{Ic} = -2.39$. The relatively small disagreement (10 % in Re_c and 4 % in λ_{Ic}) is not due to boundary conditions since we found $Re_c = 5.19$ and $\lambda_{Ic} = -2.39$ by imposing

† In Nore *et al.* (2004) the Reynolds number is given by $Re\ \Gamma^2$ and the aspect ratio by $2/\Gamma$.

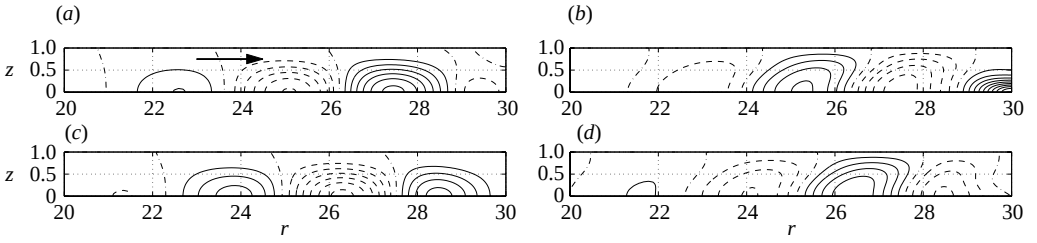

FIGURE 2. Perturbation contours with $\Gamma = 30$ and $Re = 5.16$ for: (*a*) $Re(\psi_p)$, (*b*) $Re(u_{\theta p})$, (*c*) $\mathrm{Im}(\psi_p)$, (*d*) $\mathrm{Im}(u_{\theta p})$. The solid curves are positive isovalues, the dashed curves are negative isovalues and the dash-dotted curves are the zero isovalues. The increments for isovalues are 0.01 for ψ_p and 0.1 for $u_{\theta p}$.

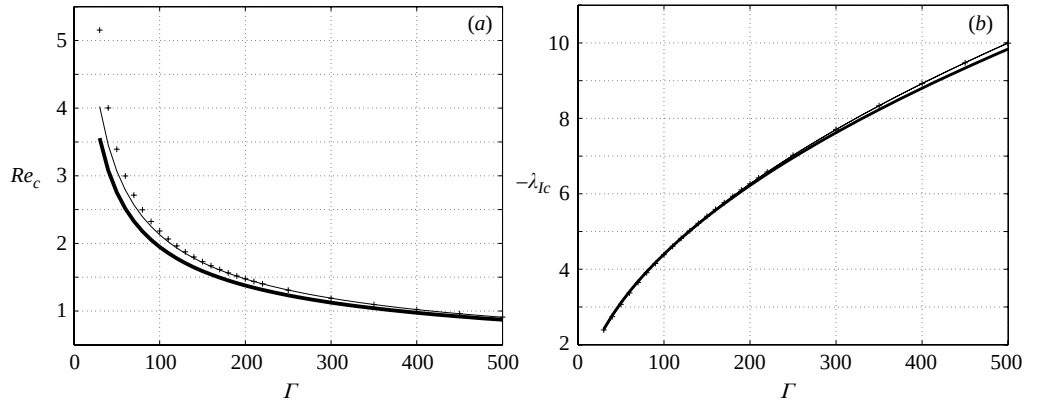

FIGURE 3. Evolution with the aspect ratio Γ of (*a*) the value of the critical Reynolds number Re_c and (*b*) the imaginary part of the eigenvalue λ_{Ic}. Symbols are for the numerical calculations and thin lines are the fit given by (2.9). Thick lines are for the predictions given by the local parallel approximation (3.8).

a no-slip condition at $r = \Gamma$ in our calculations in order to match the experimental boundary conditions.

A representation of the real and imaginary parts of the eigenvectors for the streamfunction and azimuthal velocity perturbation is shown in figure 2. We normalize the eigenvectors so that $u_{\theta p} = 1$ at $r = \Gamma$ and $z = 0$. We choose $\Gamma = 30$ but for any other aspect ratio larger than 30, the patterns are similar. We computed on the full domain but only show part of the domain as the amplitude of the perturbation rapidly decays with decreasing r.

The values of the critical Reynolds numbers Re_c and the imaginary part of the eigenvalue λ_{Ic} as a function of Γ are plotted in figure 3 for $\Gamma > 30$ and some of the computed values are given in table 1. We first used a full domain code, i.e. solving for $[0, \Gamma] \times [0, 1]$; then for larger values of Γ, we truncated the domain so that we only solved for $[\Gamma - 20, \Gamma] \times [0, 1]$. In order to check the influence of the boundary conditions (2.5)–(2.7), both the full and truncated domain codes have been used for $30 \leqslant \Gamma \leqslant 150$. We found that truncating the domain did not affect significantly the values of the critical Reynolds number nor the imaginary part of the eigenvalue. The differences were at most 0.3 %. By fitting our results for large values of Γ ($\Gamma \geqslant 200$), we found the following approximate scaling:

$$Re_c \sim 24.3\Gamma^{-0.53} \quad \text{and} \quad \lambda_{Ic} \sim -0.42\Gamma^{0.51}. \tag{2.9}$$

Γ	Re	$-\lambda_{Ic}$	Γ	Re	$-\lambda_{Ic}$	Γ	Re	$-\lambda_{Ic}$	Γ	Re	$-\lambda_{Ic}$
2	27.3	0.	26.6	5.89	0.	100	2.19	4.38	300	1.19	7.71
4	15.0	0.	26.7	5.86	2.28	150	1.73	5.39	350	1.10	8.34
10	9.22	0.	30	5.16	2.39	200	1.48	6.26	400	1.02	8.92
20	6.67	0.	50	3.39	3.07	250	1.31	7.02	500	0.91	9.99

TABLE 1. Values for the critical Reynolds number and the critical frequency for different aspect ratios Γ. In all cases, the antisymmetric mode is critical.

The scaling for the critical Reynolds number indicates that the instability mechanism cannot be explained using a simple physical argument such as a shear flow based on the maximum azimuthal velocity ΩR and a characteristic distance H between the disks. If these scales were relevant, then Re_c would scale as Γ^{-1}.

3. Local parallel approximation

In this section, we show that the instability is driven not by the end region but by the core region of the system. More precisely, we claim that the instability that takes place near the end region does not stem from the strong return base flow but is driven by the core flow for which the velocities are maximum at the edge of the core region.

The key ingredient of the instability can be captured by considering two infinite disks and viewing Γ as a local radius associated to a local Reynolds number $\hat{R}e$.

3.1. *Asymptotic analysis for large Γ*

In order to find an asymptotic expansion in the vicinity of the local radius Γ for large values of Γ, we introduce the following coordinate change and rescaling:

$$r = \Gamma + x \quad \text{and} \quad Re = \hat{R}e\,\Gamma^{-1/2}. \tag{3.1}$$

From (2.8), the leading-order terms in the core region for the base azimuthal velocity and the base streamfunction are

$$\Gamma\hat{u}_{\theta b} \quad \text{and} \quad \Gamma^{3/2}\hat{\psi}_b \quad \text{with } \hat{u}_{\theta b} = z \quad \text{and} \quad \hat{\psi}_b = \hat{R}e\,f(z). \tag{3.2}$$

The perturbation variables are defined up to an arbitrary multiplicative constant, so that we choose a scale for one variable, namely we choose $u_{\theta p}$ to be $O(1)$. We rewrite (2.1)–(2.3) with the perturbation variables having the following form:

$$\psi_p(r,z)\exp(\lambda t) = (\Gamma^{\alpha}\psi_{p0}(z) + \cdots)\exp[(\Gamma^{\gamma}\lambda_0 + \cdots)t + \mathrm{i}kx], \tag{3.3}$$

$$u_{\theta p}(r,z)\exp(\lambda t) = (\Gamma^{0}u_{\theta p0}(z) + \cdots)\exp[(\Gamma^{\gamma}\lambda_0 + \cdots)t + \mathrm{i}kx]. \tag{3.4}$$

In order to retain the maximum number of terms of order ϵ, the least restrictive choice for the unknown powers of Γ are $\alpha = -1$ and $\gamma = 1/2$. The decomposition of the perturbation variables in elementary waves in the radial direction with a wavenumber k reduces the system to ordinary differential equations so that (2.1)–(2.3) at respective order $\epsilon\Gamma^{-1}$, $\epsilon\Gamma^{-1/2}$ and $\epsilon\Gamma^{1/2}$ become

$$\lambda_0\omega_{p0} + \hat{R}e\,f'\mathrm{i}k\omega_{p0} - \hat{R}e\,f'''\mathrm{i}k\psi_{p0} - 2(z\,u_{\theta p0})' = \frac{1}{\hat{R}e}(-k^2\omega_{p0} + \omega''_{p0}), \tag{3.5}$$

$$-k^2\psi_{p0} + \psi''_{p0} = \omega_{p0}, \tag{3.6}$$

$$\lambda_0 u_{\theta p0} - \mathrm{i}k\psi_{p0} + \hat{R}e\,f'\mathrm{i}ku_{\theta p0} = \frac{1}{\hat{R}e}(-k^2u_{\theta p0} + u''_{\theta p0}), \tag{3.7}$$

where primes denote differentiation with respect to z. The boundary conditions are $u_{\theta p0} = \psi_{p0} = \psi'_{p0} = 0$ at $z = 1$ and symmetric or antisymmetric conditions at $z = 0$.

3.2. *Local instability results*

We solve these Orr–Sommerfeld-type equations using a technique similar to that used for the complete partial differential equations. The grid has 61 points evenly spaced in the z-direction. For a given real value of k we search for the values of the critical Reynolds number. The minimum critical Reynolds number $\hat{R}e = 19.5$ is found to be reached at $k = 1.12$. The corresponding frequency is $\lambda_{I0c} = -0.44$. Qualitatively, the perturbations are antisymmetric and reproduce the patterns found in figure 2. Quantitatively, the critical Reynolds number Re_c and frequency λ_{Ic} are

$$Re_c \sim 19.5\Gamma^{-1/2} \quad \text{and} \quad \lambda_{Ic} \sim -0.44\Gamma^{1/2}, \tag{3.8}$$

to be compared with those reported in (2.9).

When comparing the asymptotic prediction (3.8) with the values in table 1, the two frequencies λ_{Ic} are in excellent agreement (within 2 %) whereas the critical Reynolds number Re_c is lower by up to 36 % (for the worst case $\Gamma = 26.6$). The difference drops below 11 % when $\Gamma > 100$. The asymptotic model proposed is valid only for large enough values of Γ and the underestimation can be explained by the fact that this one-dimensional model does not take into account the stabilizing effect of the end region. The closed end condition $\psi = 0$ at $r = \Gamma$ strongly modifies the azimuthal velocity u_θ and therefore weakens the source of the instability.

As an illustration, we can compare an evaluation of the phase velocity for $\Gamma = 30$ with the asymptotic prediction. For the full (as well as the truncated) domain calculations, the spatial wavenumber in the radial direction varies (moderately) with the radius so that the phase velocity is at best a rough approximation. From figure 2 we found a spatial wavelength of ~ 5.5 so that the phase velocity $-\lambda_I/k \sim 2.39 \times 5.5/(2\pi) \sim 2.1$. The phase velocity for the local model is given by $-\lambda_{I0c}/k$ which satisfactorily yields $0.44\sqrt{30}/1.12 \sim 2.2$ if we rescale the frequency according to (3.8).

In the locally parallel approximation, the convective/absolute nature of the flow can also be determined. To do so, we have to solve (3.5)–(3.7) for complex wavenumber k with a prescribed complex frequency λ_0. The flow is found to be convectively unstable in a very narrow Reynolds number range $\hat{R}e_c = 19.5 < \hat{R}e < \hat{R}e_{ca} = 19.7$. The Reynolds number $\hat{R}e_{ca}$ at which the flow becomes absolutely unstable has been determined by standard saddle-point tracking and checking that, in the complex k-plane, pinching occurs between the k^- and k^+ branches. The critical mode has wavenumber $k_{ca} \approx 1.26 - 0.08\mathrm{i}$ and a frequency $\lambda_{I0_{ca}} = -0.45$.

We found that the meridional flow, which has only a radial component at leading order, does not play a key role in the destabilizing mechanism and in fact slightly stabilizes the flow. If we artificially set $f(z)$ (defined in (2.8)) and its derivatives to zero in (3.5) and (3.7), the critical Reynolds is lowered to $\hat{R}e_c = 15.4$ for $k = 1.08$ and the frequency is shifted to $\lambda_{I0c} = -0.36$ but the features of the instability are unchanged. In what follows, we disregard this radial component of the base flow in order to understand the physical mechanism of the instability.

3.3. *Physical mechanism*

If we retain only the key terms for the perturbation, the equations can be approximated by

$$\frac{\partial \omega^\star}{\partial t} = 2\frac{\partial(\hat{u}_{\theta b}\, u^\star_\theta)}{\partial z} + \text{diff. terms} = 2\frac{\partial(z\, u^\star_\theta)}{\partial z} + \text{diff. terms}, \tag{3.9}$$

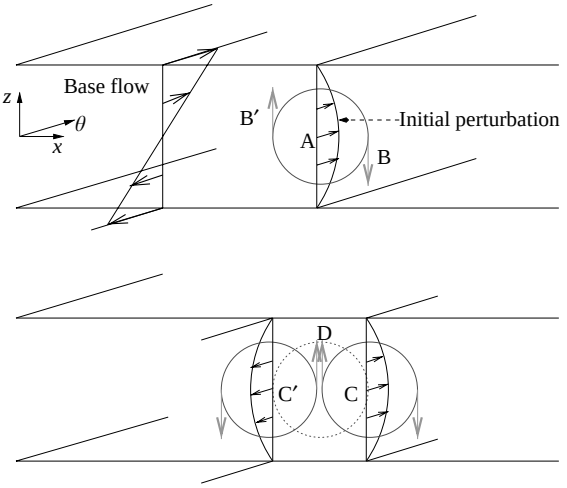

FIGURE 4. Schematic mechanism for the instability over half of a period.

$$\frac{\partial u_\theta^\star}{\partial t} = -u_z^\star \frac{\mathrm{d}\hat{u}_{\theta b}}{\mathrm{d}z} + \text{diff. terms} = -u_z^\star + \text{diff. terms}, \tag{3.10}$$

where the starred variables represent the real perturbation variables. These time evolution equations are equivalent to (3.5) and (3.7) with $f(z) = 0$ and clearly show the competition between convective (or source) and diffusive terms. In addition to these equations, there is a relation between $\omega^\star$ and $\psi^\star$ that can be deduced from (2.2).

In figure 4, we illustrate how the coupling between (3.9) and (3.10) will amplify and propagate a small perturbation. An initial positive and even azimuthal velocity perturbation A is the source for locally positive vorticity (not represented) at the symmetry plane (see (3.9)). Positive vorticity induces a clockwise circulation and therefore the axial velocities B and B′. As indicated by (3.10), convection of the base flow by axial velocity is a source term for the azimuthal velocities C and C′. The initial pattern (B′AB) has propagated in the radial direction toward the periphery and a counterclockwise circulation has been generated toward the axis. We have then completed a quarter of a period. At the point where the perturbation originated, the two circulations contribute to a positive axial velocity D with a stronger intensity. Equation (3.10) indicates that this will create a negative azimuthal velocity (not represented) and therefore a counterclockwise circulation (dashed). We have then completed half a period. The other half is easily deduced with the appropriate changes in signs. Moreover this mechanism is thought to be also indicative of the inward (from A to C′) and outward (from A to C) spreading of energy, suggesting absolute instability. It should be noted that contrary to the plane Couette flow invariant under spanwise reflection, the present model includes a centrifugal acceleration that breaks this symmetry. More specifically, the source term in (3.9) derived from the centrifugal acceleration imposes a positive phase velocity (or outward motion) on the structures.

3.4. *Recovering the spatial radial inhomogeneity from the local study*

In this section, we use local stability properties deduced from the asymptotic analysis of § 3.1 in order to recover the envelope of the global instability mode obtained in § 2.2 in the limit of large aspect ratios Γ. The scaling (3.1) indicates that a local Reynolds number is defined as: $Re_l(r) \equiv r^{1/2} Re = \Omega H^{3/2} r_\mathrm{d}^{1/2}/\nu$ where r_d is

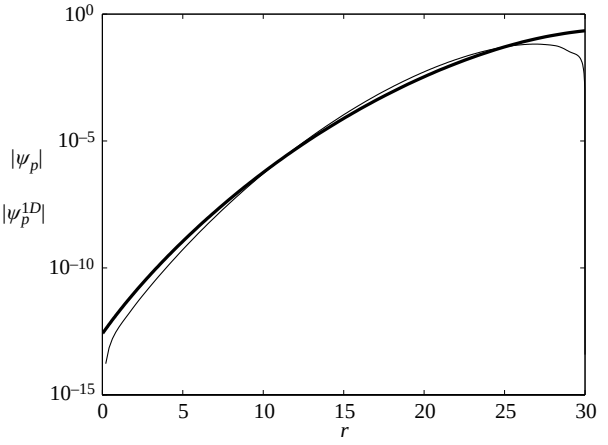

FIGURE 5. Comparison of the perturbation amplitude for the streamfunction at $z = 0$. The thin line $|\psi_p|$ corresponds to the envelope of the global mode ψ_p presented in figure 2. The thick line $|\psi_p^{1D}|$ is obtained by integration of (3.11) and the arbitrary multiplicative constant is chosen so that $|\psi_p| = |\psi_p^{1D}|$ at $r = 25$.

the dimensional radius. This local Reynolds number virtually vanishes at the axis and increases with r. Thus, a central region exists where the flow is locally stable, bearing only evanescent waves. As the instability source necessarily lies close to the end region, the global mode envelope, in the central region, is locally given by the spatial growth rate k_I^-. In this linear framework, the selected frequency is the absolute frequency $\lambda_{I0}^{\mathrm{abs}}$ of the local mode at $r = \Gamma$ (Monkewitz, Huerre & Chomaz 1993). Here, we take $\lambda_{I0}^{\mathrm{abs}} = \lambda_{I0_{ca}} = -0.45$. Neglecting non-parallel effects, the numerical integration of

$$\frac{1}{\left|\psi_p^{1D}\right|}\frac{\mathrm{d}\left|\psi_p^{1D}\right|}{\mathrm{d}r} = -k_I^- \tag{3.11}$$

where k_I^- is evaluated at $Re_l(r)$ allows us to recover the envelope of the global mode ψ_p. As shown in figure 5, there is a fair agreement between $|\psi_p^{1D}|$ and $|\psi_p|$ in the core region except close to the axis where, not surprisingly, the hypothesis $r = O(\Gamma)$ does not hold. The discrepancy in the end region is due to the fact that this one-dimensional local model does not take into account the closed end of the real geometry.

4. Conclusions

We have presented a numerical study of the first bifurcation for counter-rotating disks for arbitrarily large but finite aspect ratio. These axisymmetric computations are in good agreement with experiment for $\Gamma = 30$. The scaling law for the critical Reynolds number and the critical frequency as a function of Γ is found. The comparison of the truncated and the full domain computations in § 2 shows that the source for the instability is close to the end region. Nevertheless, in § 3, using an asymptotic model, we show that the physics of the instability can be completely understood with a one-dimensional model and that it is generated in the core region where the base flow has a simple analytical expression. More specifically, we show that the key term is the centrifugal acceleration which is always of the same order of magnitude as the diffusive terms for $Re = Re_c$. This latter remark implies that

a centrifugal instability will always occur no matter how large the local radius considered, which distinguishes it from the plane Couette flow.

We thank Emilie Delisle, Eric Foucault, Patrice Le Gal, Caroline Nore, Benoît Pier, Laurette Tuckerman and Shihe Xin for fruitful discussions.

REFERENCES

Batchelor, G. K. 1951 Note on a class of solutions of the Navier-Stokes equations representing steady rotationally-symmetric flow. *Q. J. Mech. Appl. Maths* **4**, 29–41.

Fernandez-Feria, R. 2000 Axisymmetric instabilities of Bödewadt flow. *Phys. Fluids* **12**, 1730–1739.

Gauthier, G., Gondret, P., Moisy, F. & Rabaud, M. 2002 Instabilities in the flow between co- and counter-rotating disks. *J. Fluid Mech.* **473**, 1–21.

Gelfgat, A. Y., Bar-Yoseph, P. Z. & Solan, A. 1996 Steady states and oscillatory instability of swirling flow in a cylinder with rotating top and bottom. *Phys. Fluids* **8**, 2614–2625.

Harriott, G. M. & Brown, R. A. 1984 Flow in differentially rotated cylindrical drop at moderate Reynolds number. *J. Fluid Mech.* **144**, 403–418.

Hoffmann, N., Busse, F. H. & Chen, W. L. 1998 Transitions to complex flows in the Ekman–Couette layer. *J. Fluid Mech.* **366**, 311–331.

Lingwood, R. J. 1997 Absolute instability of the Ekman layer and related rotating flows. *J. Fluid Mech.* **331**, 405–428.

Martin Witkowski, L. & Walker, J. S. 2002 Solutocapillary instabilities in liquid bridges. *Phys. Fluids* **14**, 2647–2656.

Monkewitz, P. A., Huerre, P. & Chomaz, J. M. 1993 Global linear stability analysis of weakly non-parallel shear flows. *J. Fluid Mech.* **251**, 1–20.

Nore, C., Tartar, M., Daube, O. & Tuckerman, L. S. 2004 Survey of instability thresholds of flow between exactly counter-rotating disks. *J. Fluid Mech.* **511**, 45–65.

Schouveiler, L., Le Gal, P. & Chauve, M. 2001 Instabilities of the flow between a rotating and a stationary disk. *J. Fluid Mech.* **443**, 329–350.

Serre, E., Tuliszka-Sznitko, E. & Bontoux, P. 2004 Coupled numerical and theoretical study of the flow transition between a rotating and a stationary disk. *Phys. Fluids* **16**, 688–706.

Soong, C. Y., Wu, C. C., Liu, T. P. & Liu, T. P. 2003 Flow structure between two co-axial disks rotating independently. *Expl. Therm. Fluid Sci.* **27**, 295–311.

Szeto, R. K. H. 1978 The flow between rotating coaxial disks. PhD thesis, California Institute of Technology, Pasadena.